Accepted: 6 August 2022

DOI: 10.1002/lsm.23595

PRECLINICAL REPORTS

# Guide mapping for effective superficial photothermal coagulation of the esophagus using computer simulations with ex vivo sheep model validation study

**Merve Turker-Burhan BS**[1,2] | **Nevin Ersoy PhD**[3] | **Husnu A. Bagriyanik MD, PhD**[1,3] | **Serhat Tozburun PhD**[1,2,4]

[1]Izmir Biomedicine and Genome Center, Izmir, Turkey

[2]Izmir International Biomedicine and Genome Institute, Dokuz Eylul University, Izmir, Turkey

[3]Department of Histology and Embryology, Faculty of Medicine, Dokuz Eylul University, Izmir, Turkey

[4]Department of Biophysics, Faculty of Medicine, Dokuz Eylul University, Izmir, Turkey

**Correspondence**

Serhat Tozburun, PhD, Izmir International Biomedicine and Genome Institute, Dokuz Eylul University, Izmir 35340, Turkey.
Email: serhat.tozburun@deu.edu.tr

**Funding information**

Türkiye Bilimsel ve Teknolojik Arastirma Kurumu, Grant/Award Number: 117E985; H2020 Marie Sklodowska-Curie Actions, Grant/Award Number: 835907

## Abstract

**Objectives:** The transfer and widespread acceptance of laser-induced thermal therapy into gastroenterology remain a topic of interest. However, a practical approach to the quantitative effect of photothermal injury in the esophagus needs further investigation. Here, we aim to perform computer simulations that simulate laser scanning and calculate the laser-induced thermal damage area. The simulation engine offers the results in a guide map for laser coagulation with a well-confined therapeutic area according to laser irradiance and surface scanning speed. The study also presents validation experiments that include histology analyses in an ex vivo sheep esophagus model.

**Methods:** The simulation engine was developed based on the Monte-Carlo method and the Arrhenius damage integral. The computational model mimicked laser scanning by shifting the position of the calculated heat source in the grating system along the axis to be scanned. The performance of the simulations was tested in an ex vivo sheep esophagus model at a laser wavelength of 1505 nm. Histological analysis, hematoxylin–eosin staining, light microscope imaging, and block-face scanning electron microscopy were used to assess thermal damage to the tissue model.

**Results:** The developed simulation engine estimated the photothermal coagulation area for a surface scanning speed range of 0.5–8 mm/second and laser power of up to 0.5 W at a 0.9-nm laser diameter in a tissue model with a volume of $4 \times 4 \times 4\,mm^3$. For example, the optimum laser irradiation for effective photothermal coagulation in the mucosa and superficial submucosa depths was estimated to be between 16.4 and 31.8 $W/cm^2$, 23.2 and 38.1 $W/cm^2$ at 0.5 and 1 mm/second, respectively. The computational results, summarized as a guide map, were directly compared with the results of ex vivo tissue experiments. In addition, it was pointed out that the comparative theoretical and experimental data overlap significantly in terms of energy density.

**Conclusions:** Our results suggest that the developed simulation approach could be a seed algorithm for further preclinical and clinical trials and a complementary tool to the laser-induced photothermal coagulation technique for superficial treatments in the gastrointestinal tract. In future preclinical studies, it is thought that the simulation engine can be enriched by combining it with an in vivo model for different laser wavelengths.

**KEYWORDS**

esophageal mucosa, laser coagulation, laser therapy, Monte-Carlo simulations

  

# INTRODUCTION

Of the four layers (mucosa, submucosa, muscularis externa, and serosa) that constitutes the gastrointestinal wall,[1] the mucosa is the first tissue layer to be accessed in endoscopic procedures. This structure facilitates minimally invasive treatment of mucosal lesions when necessary in certain critical cases, as precancerous mucosal lesions are associated with gastrointestinal tract malignancies (e.g., esophageal cancer, gastric cancer, colon cancer, and rectal cancer).[2] In surgical treatments, endoscopic therapeutic interventions are widely used to eliminate abnormal mucosal tissue (e.g., Barrett's esophagus, a precancerous esophagus condition)[3] that may spread to deeper tissue structures over time. Endoscopic mucosal resection and endoscopic thermal therapy are generally accepted treatment methods among these interventions.

We can list various techniques for endoscopic thermal therapy,[3–5] such as multipolar electrocoagulation, radiofrequency (RF) ablation, argon plasma coagulation, cryotherapy, and photothermal coagulation. RF ablation and argon plasma coagulation are two noticeable techniques for exposing the tissue to heat energy. In RF ablation, the delivery of high-frequency alternating current (350–500 kHz) through electrodes in direct contact with tissue provides heat generation for thermal injury.[6] Argon plasma coagulation inflicts thermal damage to the target tissue by transmitting high-frequency energy through argon gas flow to induce heat generation in a noncontact manner.[7]

However, although endoscopic therapeutic interventions efficiently eradicate superficial abnormal tissues, the main challenge with their current deployments is that the therapy depth typically has a more profound thermal injury than the target layer.[8] This unintentional failure of possible thermal damage, coupled with multiple treatment sessions, results in organ narrowing, bleeding, or perforation. To address this challenge, an approach that provides a limited depth of the thermal effect to the epithelial layer (~500 μm thick),[9,10] particularly at the micrometer scale, may be of interest. With the latest developments in fiber optic components and diode laser technologies, laser-induced photothermal coagulation (i.e., laser therapy method) may once again come to the fore as the closest approach.

Photothermal coagulation uses laser radiation to deliver heat energy to the esophageal mucosal lining. The primary mechanism is to match the laser wavelength and corresponding optical penetration depth to the therapeutic depth in the targeted layer. In this context, various laser types and laser wavelengths have been tried before in mucosal ablation applications.[11–16] Despite some limitations, these studies have shown promising results in clinical settings. However, the treatment parameters, including laser irradiance, surface scanning speed, and laser energy density, provide a relatively sizeable variable matrix that must be optimized for consistent and reliable superficial treatment. Besides, these critical parameters have been chosen empirically without adequate comparison with the theory in the literature. Therefore, it may be necessary to develop a simulation algorithm (i.e., simulation engine) that simulates photothermal coagulation of esophageal layers in optimizing the parameters.

This study presents computer simulations that calculate a guide map of the area of irreversible thermal damage at a well-confined depth. The map simplified a matrix of laser irradiance, beam diameter, and surface scanning speed for successful superficial laser therapy. The study also included validation of the map in an ex vivo sheep model using a 1505-nm laser operated in continuous-wave (CW) mode with constant beam diameter.

# MATERIALS AND METHODS

## Laser-induced photothermal coagulation simulations

A simulation engine was developed to examine the matrix formed by the laser irradiance and surface scanning speed parameters, mainly to calculate the wavelength-dependent, depth-resolved photothermal coagulation area (i.e., the laser-induced thermal damaged area). Figure 1 shows the block flowchart of the four-module model. The first module was based on the Monte-Carlo technique[17,18] using the multilayer approach and estimated the three-dimensional (3D) photon weight distribution of an infinitely narrow photon beam with circular symmetry. The calculation corresponded to the probability of absorption and scattering events. In light propagation with randomly sampled step sizes, the events at each step were described by the following wavelength-dependent optical properties: absorption coefficient, scattering coefficient, relative refractive index, and anisotropy factor.

In the second module, the calculated photon weight distribution was interpolated on a 3D grid in the Cartesian coordinate system, normalized to 1 in power, and convolved to derive a Gaussian laser beam profile. Thus, the power density was estimated as a function of the grid system and beam diameter inputs. The physical size of the single-layer, homogeneous tissue model was 4 mm in all axes ($x$,$y$,$z$). A uniform grid system (i.e., $100 \times 100 \times 100$) with a mesh size of $40 \times 40 \times 40\,\mu m^3$ constituted the 3D structure. The thickness of the tissue sample was determined to be 4 mm, which is the sum of mucosal layer thickness (0.54 mm), submucosal layer thickness (0.55 mm), muscularis layer thickness (0.63 mm), and muscle layer (>2 mm).[9] The third module simulated the time-dependent heat diffusion generated by laser power density (i.e., laser irradiance) utilized as a heat source. The numerical model of heat diffusion was based on a partial differential equation governed by the heat transfer laws.[19] The equation was solved by the finite difference method over time and space,

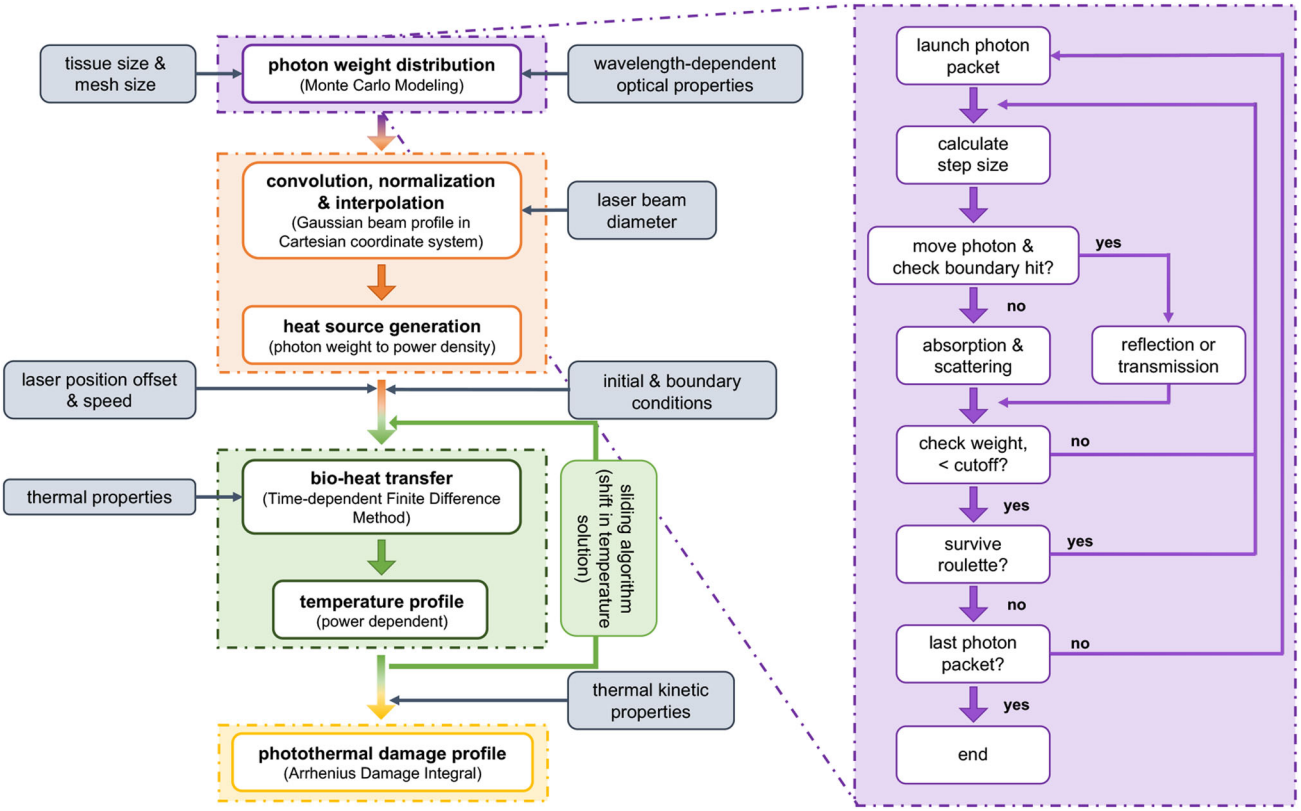


**FIGURE 1** Flowchart of the four-module simulation engine

performed on a custom-written Objective-C++ code by Xcode (Apple, Inc.)

$$\rho C\frac{\partial T}{\partial t} = k\nabla^2 T + Q, \tag{1}$$

where $\rho$ is the density, $C$ is the specific heat capacity, and $k$ is the thermal conductivity, $Q$ represents the heat source computed by using Modules 1 and 2, and $T$ is the simulated tissue temperature ($x$,$y$,$z$, *time*).

The initial position of the calculated heat source in the grid system was shifted along the axis to be scanned to mimic the scanning of laser radiation on the tissue surface. The mesh size of 40 μm was the unit shift distance. The unit time step corresponding to the calculated surface scanning speed was assigned according to the mesh size of 40 μm. For instance, the unit step time is defined as 40 ms for a 1 mm/second scanning speed and 80 milliseconds for 0.5 mm/second. To avoid discrete calculations, the partial differential equation is iteratively solved in 10 microseconds unit time, including the new boundary conditions at each heat source shift. Due to limited memory usage, a total of 1000 solutions were saved at equal intervals from the high number of iterations.

For example, Figure 2A shows representative simulation results of transient temperature calculations from the surface at selected time points from 25 milliseconds ($t_0$) to 2.5 seconds ($t_{999}$) for the scanning speed of 1 mm/second. The laser power was 309 mW, corresponding to the irradiance of 48.6 W/cm$^2$ for a fixed laser spot diameter (0.9 mm at the surface). In the calculations, the initial tissue temperature was set to 37°C. Figure 2B shows the 3D temperature distribution in the tissue model when the highest temperature 1.37 seconds ($t_{547}$) is reached during the simulation (from $t_0$ to $t_{999}$). Both surface and cross-sectional views are provided for a clear presentation of 3D transient temperature calculations. The customized color bar indicates the temperature range from 37°C to 115°C.

In the last module, laser-induced thermal damage was estimated in four-dimensions ($x$,$y$,$z$, *time*) using simulated temperature distributions for different sets of laser irradiation and surface scanning speeds, as exemplified for a single set in Figure 2. The module was based on the Arrhenius damage integral[20] to generate the thermal injury parameter (Ω) followed by a normalization factor, representing the fraction of coagulated proteins in a given volume

$$\Omega = \xi\int_0^{\tau} e^{\frac{-E_a}{RT}}dt, \tag{2}$$

where is $\xi$ the frequency factor, $\tau$ is the total heating time, $E_a$ is the activation energy of transformation, $R$ is the

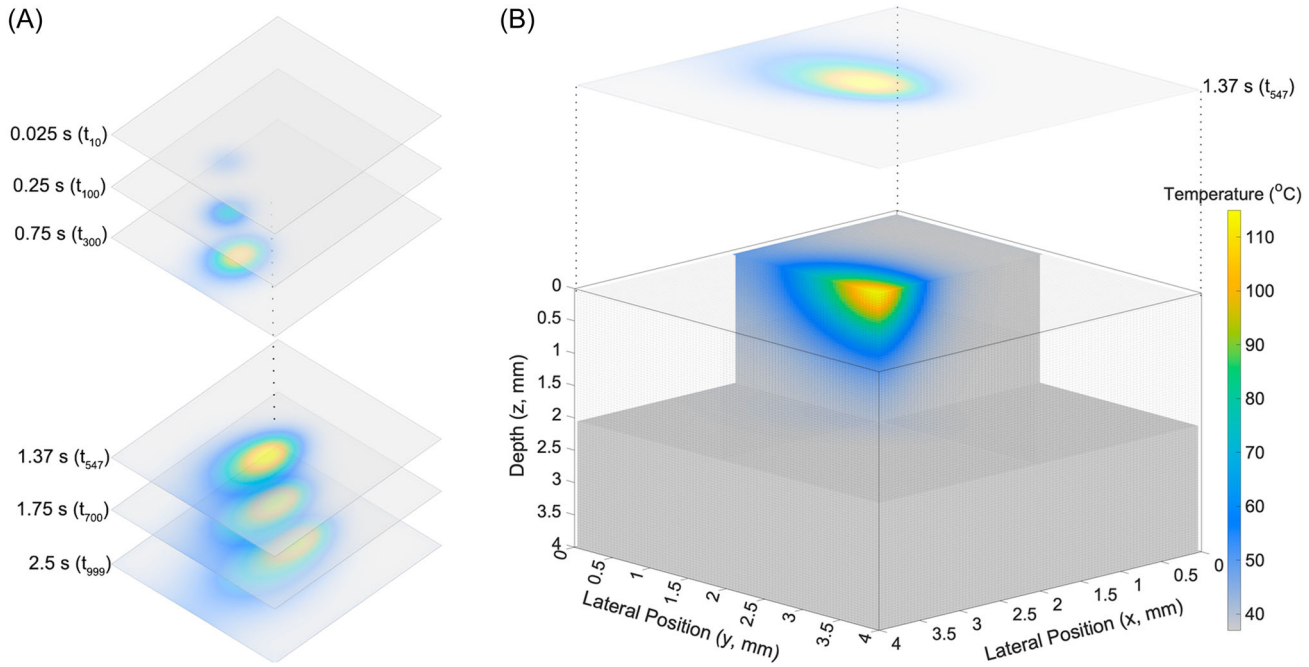


**FIGURE 2** Representative simulation results of transient temperature calculations from the surface at selected time points from 25 milliseconds ($t_0$) to 2.5 seconds ($t_{999}$) (A). Three-dimensional temporal temperature distribution in the tissue model when the highest temperature is reached during the simulation (B). The laser power is set to 309 mW, corresponding to 48.6 W/cm$^2$ radiation for a 0.9 mm beam diameter, and the surface scanning speed is 1 mm/second.

universal gas constant, and $T$ is the absolute temperature of the tissue in Kelvin.

The damage index, called the damage probability, was produced by normalizing the thermal injury parameter to 1. The damage index grade is 1, corresponding to a necrotic cell concentration of 63%, while 4.6 corresponds to a necrotic cell concentration of 99%.

The optical properties at 1505 nm, thermal properties, and kinetic coefficients of the tissue model used in the simulation were compiled from the literature (Table 1). Besides, it was assumed that the coefficients are independent of temperature changes. Body temperature was fixed to 37°C during all simulations. The total number of unit-weighted photons required to accurately simulate the absorbed radiation distribution in the tissue model with sufficient spatial resolution was determined as one million. Modules 1 and 3 of the simulation engine were developed with the C programming language. Calculations in Modules 2 and 4 and all graphical analyses of the simulation engine have been completed on MATLAB (Mathworks, Inc.).

**TABLE 1** Optical properties, thermal properties, and thermal kinetic properties used in simulation studies

| | **Tissue** |
|---|---|
| Optical properties at 1505 nm | Mucosa |
| Absorption coefficient (cm$^{-1}$) | 12[21] |
| Reduces scattering coefficient (cm$^{-1}$) | 9.5[21] |
| Anisotropy factor | 0.6[21] |
| Refractive index | 1.33 |
| Thermal properties | Esophagus |
| Thermal conductivity (W/m°C) | 0.527[22] |
| Specific heat (J/kg°C) | 3720[22] |
| Density (kg/m$^3$) | 1126[22] |
| Kinetic coefficients | |
| Frequency factor (second$^{-1}$) | 1.3e95[23] |
| Activation energy (J/mol) | 6.04e5[23] |
| Universal gas constant (J/kmol) | 8.32 |

## Experimental setup for ex vivo tissue studies

At this early stage, we planned ex vivo tissue studies as a guide, albeit limited, and thus also took into account the replacement approach of the 3Rs (replace, reduce, and refine). The sheep esophagus was chosen as the tissue model because of its easy accessibility and similarity to the human esophagus in terms of morphology and layer thickness.[24–27] All ex vivo esophageal studies were performed in a fume hood (Köttermann), which provides a biologically safe environment, as approved by the Biosafety Board of the Izmir Biomedicine and Genome Center.

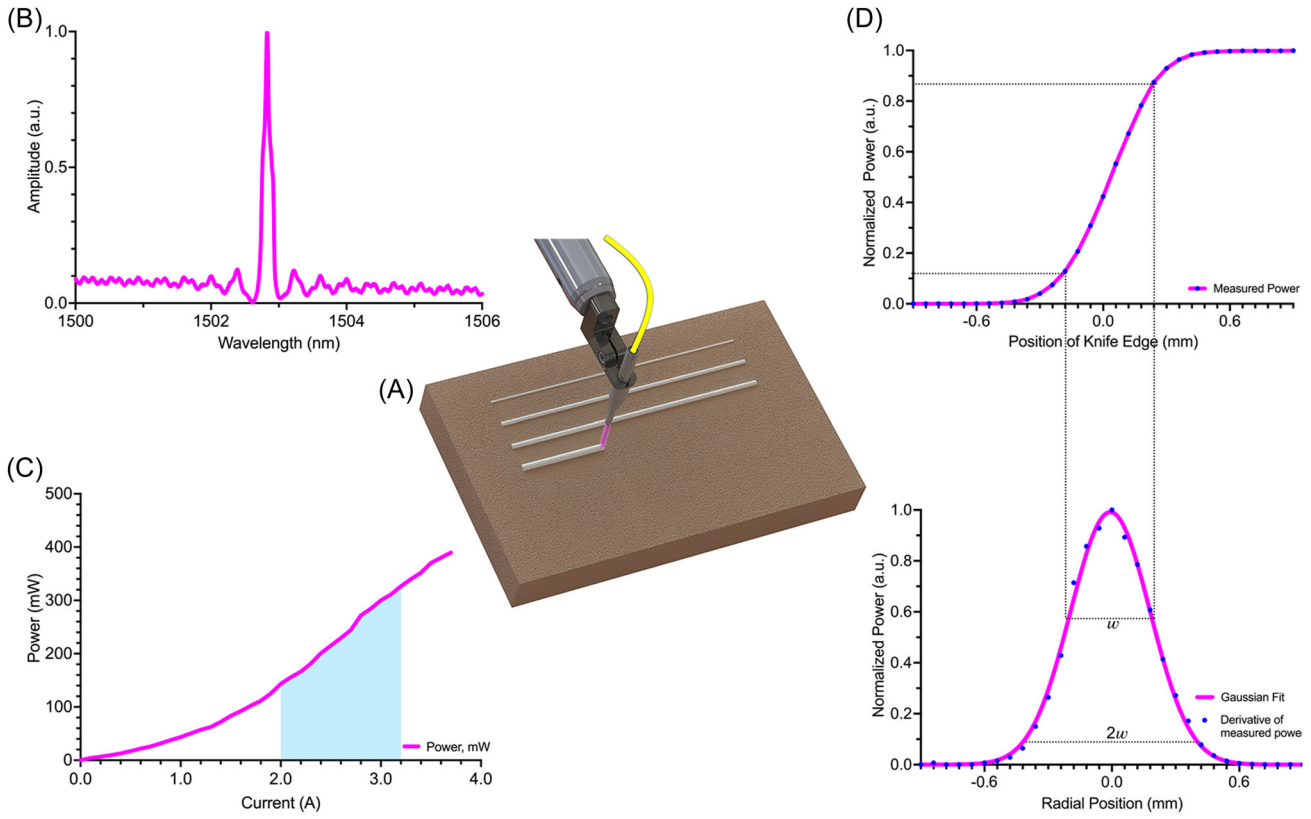


**FIGURE 3** Schematic representation of the protocol followed in ex vivo tissue studies (A). The emission spectrum of the diode laser used in the experiments (B). The wavelength was measured as 1502.83 nm. A graph of the laser output power delivered through a GRIN lens as a function of the applied electric current (C). The light blue area indicates the power range (133–309 mW) used during laser coagulation studies. Normalized laser powers along the knife-edge position and Gaussian fitted first derivatives (D). The estimated diameter of the laser beam produced by the GRIN lens using the knife-edge method was ~0.9 mm ($1/e^2$).

Figure 3A shows the protocol followed in ex vivo tissue studies. The surface of the fresh sheep esophagus, taken from the slaughterhouse, was cleaned with saline solution. We obtained a 20-mm-long rectangular form from a cylindrical structure by performing full-thickness longitudinal dissection to reach the inner surface of the esophagus. Before photothermal coagulation studies, the tissue surface was made as flat as possible with a small metal spatula. We then investigated coagulation parameters (i.e., laser power at fixed spot size, scanning speed, scanning time) with a raster scanning pattern. While the surface scanning speed was determined and kept constant in each pattern, the laser power was increased for each line. The protocol was repeated for each ex vivo tissue to explore different scanning speeds. In this context, experiments were carried out in four groups for speeds of 0.5, 1.0, 1.5, and 2.0 mm/second.

Figure 3 also presents measurements of the laser parameters used in the study in panels B, C, and D. For example, the central wavelength of the diode laser operated in CW mode was measured as 1502.83 nm (AQ6370D; Yokogawa), shown in Figure 3B. The probe produced a laser output power of up to 390 mW (Figure 3C). Output power for each scanning speed was set to a total of seven values ranging from 133 to 309 mW, as shown in the blue shaded area in Figure 3C. Using the knife-edge measurement technique, we characterized the probe, which delivers an ~0.9 mm diameter beam ($1/e^2$) on the tissue surface (Figure 3D) and maintains the beam diameter at a working distance of 20 mm. Therefore, the power range corresponded to incident irradiance values between 20.9 and 48.6 W/cm$^2$ for a fixed laser spot diameter (0.9 mm at the surface).

Figure 4 shows the experimental setup used in ex vivo studies. The setup mainly consisted of a laser source, an XYZ linear translation optomechanical stage, a hot plate, and a digital microscope. A single-mode fiber-coupled diode laser (BrightLock; QPC Lasers Inc.) emitting laser power up to 500 mW at a wavelength of 1505 nm was used as the near-infrared (near-IR) light source. We combined the laser output with a pigtailed GRIN collimator (Go4Fiber) housed in glass tubing used as a probe. Laser radiation at 1505 nm provided an optical penetration depth of >0.57 mm in water,[28] the primary chromophore for soft tissues in the near-IR spectrum. With the identical motorized micrometer actuators (Z825B; Thorlabs), the three-axis optomechanical stage provided excellent probe control across the tissue surface,

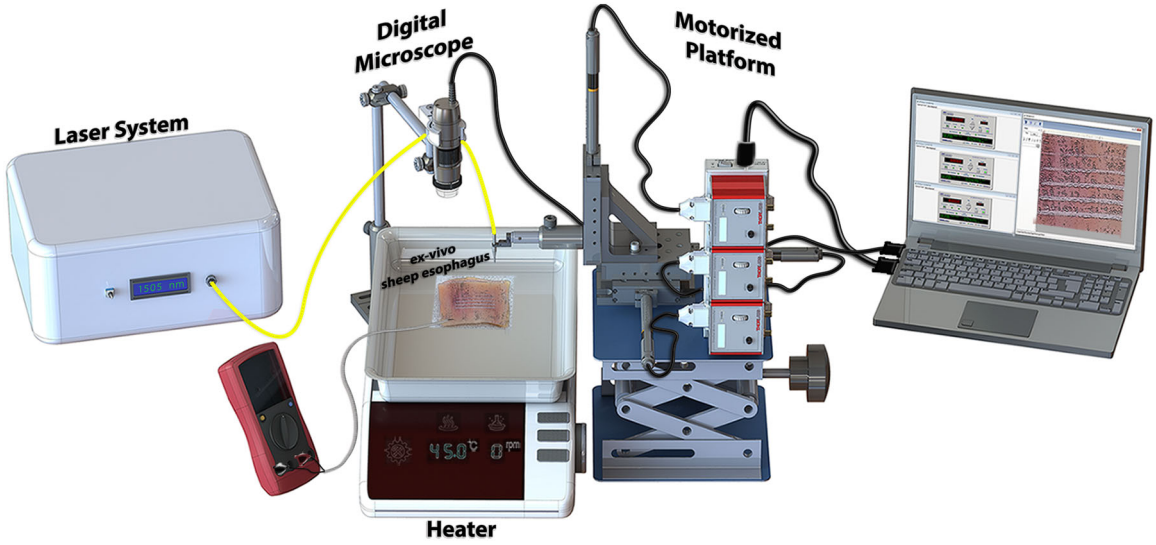


**FIGURE 4** Schematic drawing of the experimental setup used in an ex vivo sheep esophagus model. A single-mode fiber-coupled diode laser at 1505 nm is used as the near-infrared light source. The laser is coupled with a pigtailed GRIN collimator housed in glass tubing used as a probe. The setup also includes an XYZ linear translation optomechanical stage for precise control of the fiber probe across the ex vivo tissue surface, a thermocouple for instantaneous temperature measurement of the tissue, a digital microscope for alignment, and a hot plate to maintain the tissue temperature at 37°C.

parallel and perpendicular, respectively. The actuator offered a relatively accurate scanning speed of up to 2.3 mm/second with a maximum travel length of 25 mm with a step size of 0.029 µm. Ex vivo tissue at room temperature of 22°C was placed in a tray in contact with a hot plate (Thermo Fisher Scientific) set to 45°C to raise it to body temperature (37°C). We constantly checked the surface temperature with a thermocouple. A digital microscope (AM4815ZTL Dino-Lite) helped align the probe while recording the photothermal coagulation process in the invisible wavelength range.

## Histology

After the photothermal coagulation studies, tissue samples (~20 mm long) were collected to measure the depth and area of thermal damage. The collected samples were fixed in 10% neutral formalin to preserve their current state and embedded in paraffin to prepare for the sectioning process. Then, the region of interest was longitudinally sectioned from the paraffin blocks at a thickness of 5 µm. Finally, tissue processing steps were followed for standard histology analysis and electron microscopy.

For the histological study, hematoxylin–eosin (H&E) staining was performed for further microscopy examination, including brightfield and darkfield imaging. In addition, we coated some tissue sample pieces with 5-nm-thick gold using the rotary pump coating system and imaged them to support the determination of the damage boundary by electron microscopy examination.

# RESULTS

This section shows laser-induced thermal calculations based on computer simulations developed using the Monte-Carlo technique. For simplicity, we present the calculations as a guide map of the thermally damaged area as a function of two variables: laser irradiance and surface scanning speed. Various studies are then covered, including ex vivo fresh sheep esophagus experiments and histology analysis to validate the simulation results.

## Mapping photothermal coagulation of esophageal layers

In the simulation study, laser-induced thermal injury of mucosal tissue was estimated in a depth-resolved manner for various scanning speeds and laser power settings (for a fixed beam diameter of 0.9 mm, the corresponding laser beams were subsequently calculated). A guide map of the formation of the damaged area was created for easier reading of the results produced with the developed simulation engine. Figure 5 shows a map of the estimated damaged area as a function of laser irradiance (or flux density) and surface scanning speed. The map was created in three stages: first, we simulated sliding the probe along the surface of the esophagus in one direction at a constant speed. The four-dimensional (4D) temperature distribution was calculated by iteratively solving the partial differential equation (Equation 1) in 10 microseconds unit time, including the new boundary conditions at each heat source shift. As depicted in Figure 2,

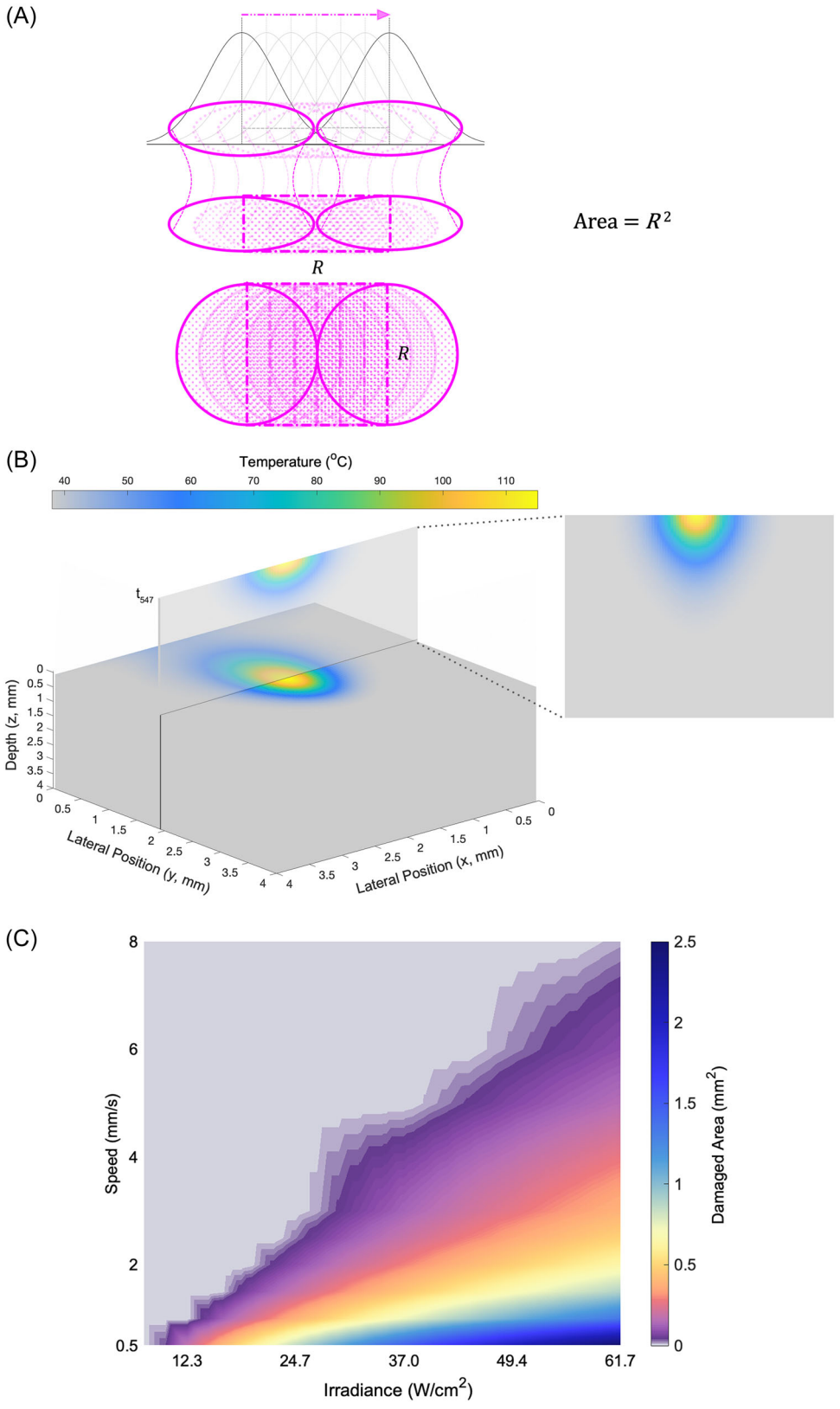


**FIGURE 5** In calculating laser irradiance, the surface area perpendicular to the beam propagation is assumed as a square given the >99% overlap of the laser beam and approximates to the square of the beam diameter (A). Surface area = $R^2$. The cross-sectional ($y,z$) solutions of the highest temperature ($T_{max}$) reached during the simulation are gathered from the calculated temperature distributions ($x,y,z$, *time*) for each surface scanning speed and laser power (B). A map of the estimated damaged area as a function of laser irradiance (i.e., flux density) and surface scanning speed (C). Laser power varies from 60 to 500 mW with a step size of 20 mW. Scanning speeds: 0.5, 1, 1.5, 2, 2.5, 3, 5, 6, and 8 mm/second. The color code represents that the damaged area varies across the graph by interpolating the calculated values for a nondiscrete data display.

a total of 1000 solutions were recorded evenly spaced from multiple iterations. The simulations were then repeated for speeds between 0.5 and 8mm/s. In the simulation of laser surface scanning at a distance of 2.5 mm, the mimicked near-IR laser exposure time was 5 seconds for 0.5 mm/s and ~0.3 seconds for 8 mm/second. At each scanning speed, the CW laser power was altered from 60 to 500 mW at a step size of 20 mW.

The surface area used in the irradiance calculation was accepted as the area scanned by the laser beam at one diameter distance. As shown in Figure 5A, the surface area perpendicular to the beam propagation was assumed to be a square given the >99% overlap of the laser beam and approximated to the square of the beam diameter (surface area = $R^2$). Therefore, the laser power from 60 to 500 mW corresponded to an irradiance range of 7.4 to 61.7 W/cm$^2$ for a 0.9 mm diameter.

The thermally damaged area was calculated from the cross-sectional temperature solutions in the transverse plane to facilitate histology analysis, which is part of the validation studies. As shown in Figure 5B, the cross-sectional ($y,z$) solutions of the highest temperature ($T_{max}$) reached during the simulation were gathered from the calculated temperature distributions ($x,y,z,$ *time*) for each surface scanning speed and laser power in the second stage. Based on temperature changes over time (i.e., gathered temperature distributions) and thermal kinetics of mucosal tissue, the laser-induced photothermal injury was defined by the concentration of necrotic cell death. The grade of damage index determined by solving the Arrhenius integral quantified the concentration of necrotic cell death. At the last stage, the damage degree index threshold was set to >0.99 to assign irreversible thermal damage. Thus, it was assumed that the tissue coagulated completely in grids with a damage index >0.99. We estimated the thermally damaged area using these designated grids with a mesh size of $40 \times 40 \times 40\ \mu m^3$.

According to the map, the optimum laser irradiance for effective photothermal coagulation at sufficient depth was estimated to be between 16.4 and 31.8 W/cm$^2$ at the lowest scanning speed of 0.5 mm/second, and between 23.2 and 38.1 W/cm$^2$ at 1 mm/second in a single axis. The highest damaged area was calculated as 2.514 mm$^2$ for 0.5 mm/second at 61.7 W/cm$^2$. For scanning speeds above 1 mm/second with all laser powers, the calculated damage area was below 0.9 mm$^2$. Besides, it was estimated that 7.7 W/cm$^2$ laser irradiation at 1505 nm wavelength did not cause mucosal tissue damage for all scanning speeds.

## Ex vivo tissue studies

We performed ex vivo tissue studies to examine the accuracy of the created guide map. The analysis included laser scanning in an ex vivo sheep esophagus model at four scanning speeds (0.5, 1.0, 1.5, and 2.0 mm/second) for seven different power settings (133, 150, 188, 220, 258, 284, and 309 mW) with the setup described in Figure 4. Laser powers corresponded to the irradiance of 16.4, 18.5, 23.2, 27.2, 31.9, 35.1, and 38.1 W/cm$^2$, respectively, for laser beam overlapping of >99% (i.e., surface area = $R^2$). The tissue was moistened with saline solution during the experiments to prevent the ex vivo sheep esophagus from drying out. Therefore, we assumed that the percentage of water did not change significantly, and the absorption coefficient of the tissue model was as constant as possible.

Figure 6A shows an example of mucosal whitening seen in gross anatomy, corresponding to thermally induced visual changes in tissue during 1 mm/second laser surface scanning. It has been hypothesized that coagulation necrosis causes such optically detectable changes in soft tissue. Note that the whitening thickness increased as a function of laser irradiance at fixed scanning speed. In comparison, it decreased relatively with increasing scanning speed at constant laser irradiance.

Samples collected at the end of the experiment were used for (1) light and (2) electron microscopy examinations to assess thermal damage to biological tissues further. Thus, in addition to observing whitening, the examination identified morphological changes in the context of evaluation response to photothermal coagulation therapy. The region of interest (magenta dashed line in Figure 6A) was sectioned from the paraffin-embedded sample blocks. Figure 6B,C shows cross-sectional histological images of H&E-stained tissue. The images were created by merging 27 images acquired at ×4 magnification in the brightfield and darkfield side by side. The primary difference between coagulated and uncoagulated areas was the hue. This difference was expressed separately by the esophageal layers.

In the brightfield image shown in Figure 6B, the epithelium became lighter while the connective tissue darkened if affected by photothermal coagulation. Indeed, the characterized morphological changes justified the color differences. Disruption of intercellular junction integrity, formation of intracellular spaces, and loss of cell contours gave the epithelium a transparent-blurry appearance, resulting in a light pink manifestation. Starting with a laser power of 188 mW, epithelium dissociation from the basal lamina occurred, although the entire stratum corneum remained intact. On the other hand, a homogenized and opaque dark pink-purple manifestation was obtained due to protein degradation in the connective tissue (lamina propria and submucosa). The darker color was probably caused by the high affinity of the free amino groups of the degraded proteins to eosin. As with surface whitening, structural changes at depth were proportionally associated with increased irradiance at constant beam diameter and decreased scanning speed (i.e., increased energy density, J/cm$^2$).

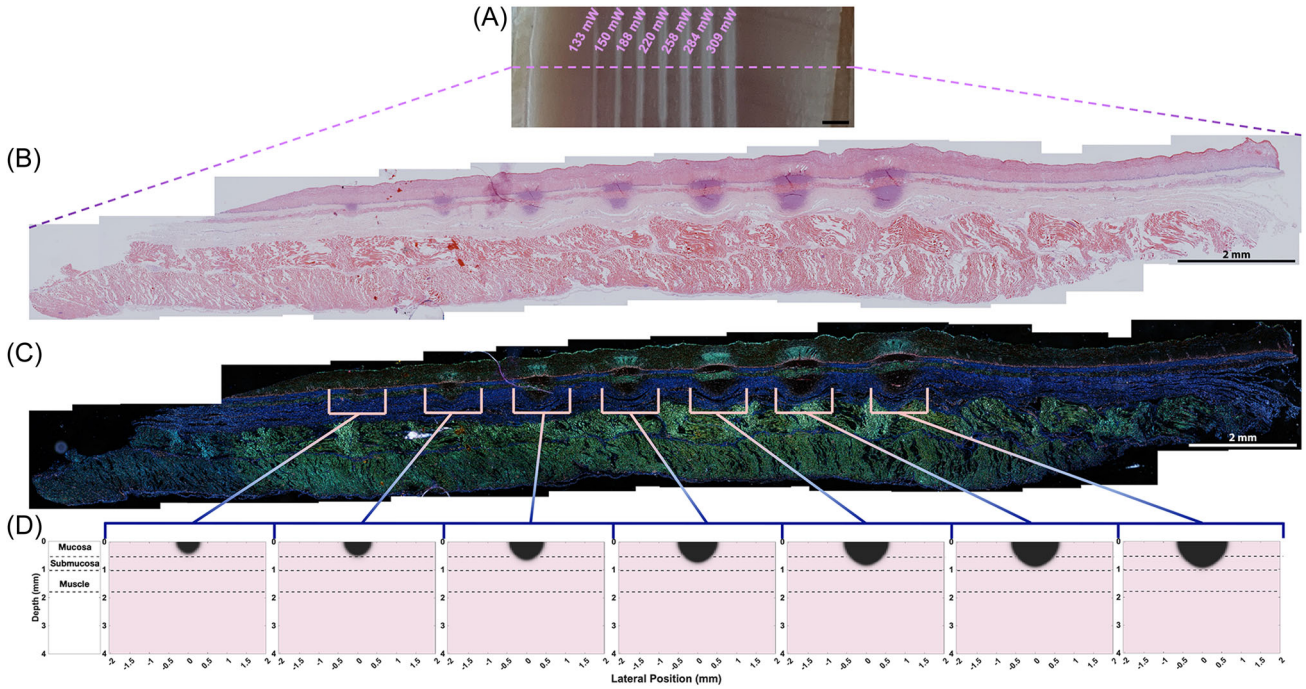


**FIGURE 6** Photograph of visible thermal damage (mucosal whitening) after laser irradiation of sheep esophagus, ex vivo (A). Wavelength = 1505 nm, laser power = 133, 150, 188, 220, 258, 284, and 309 mW, surface scanning speed = 1 mm/second. Scale bar = 2 mm. Brightfield (B) and darkfield (C) microscopy images of ex vivo sheep esophagus stained with hematoxylin and eosin. The images show the merging of 27 images acquired at ×4 magnification (0.13 NA). Laser-induced thermal damage results, which are generated by the simulation engine for seven laser powers at a scanning speed of 1 mm/second (D). Tissue damage areas are marked with black contrast to light pink. Measured thermal injury depths were approximately 0.40, 0.66, 0.74, 0.82, 0.92, 1.00, and 1.08 mm. The corresponding simulation calculations were 0.36, 0.56, 0.68, 0.76, 0.84, 0.92, and 0.96 mm, respectively.

Darkfield microscopy images of the same H&E-stained sample were obtained, as shown in Figure 6C. In darkfield imaging, which excludes unscattered light, the original hue of the stain, the thickness of the tissue sample, and the tissue density all affected the color perceived from the specimen. Dense pieces of tissue tended to reflect light more than refracting it and appear darker accordingly. In contrast, softer tissues refracted light more and shifted wavelengths significantly. As a result, a more distinct image can be acquired with different colors representing individual esophageal tissue layers; for example, the cell nucleus is in red, the muscle and cell membrane are in shades of green, and the connective tissue is in blue. The black appearance of the coagulated areas of the connective tissue in the lamina propria and submucosa layers can be explained by the tissue's relatively homogeneous and opaque formation.

Figure 6D shows the corresponding laser-induced thermal damage results of the simulation studies for seven laser powers at a scanning speed of 1 mm/second, and areas of tissue damage are marked with black. Although the tissue model was constructed as a single layer for the simulation study, the effect of photothermal coagulation on depth was estimated if the thicknesses of the esophageal tissue layers[9] were assigned accordingly. Damaged tissue depth was limited within the mucosa for 133 and 150 mW, and in the submucosa without affecting the muscle layer for 188, 220, 258, 284, and 309 mW, as seen in Figure 6—the depth and extent of tissue damage as a function of increasing power values correlated with experimental results. For example, thermal injury depths were measured approximately 0.40, 0.66, 0.74, 0.82, 0.92, 1.00, and 1.08 mm, while the corresponding simulation results were 0.36, 0.56, 0.68, 0.76, 0.84, 0.92, and 0.96 mm.

The darkfield microscopy image lacked structural details, although it increased contrast and distinguished individual tissue fragments. Therefore, we mathematically subtracted the brightfield microscope from the darkfield microscope to obtain a high-contrast image with morphological details. Figure 7 shows samples of the brightfield (A) and darkfield (B) microscope images and the subtraction result (C) for 284 mW laser power (35.1 W/cm$^2$) at a laser scanning speed of 1 mm/second. With a color subtraction approach (e.g., magenta − red = blue), uncoagulated (i.e., pink in epithelial and muscularis mucosa, yellow-orange in lamina propria and submucosa) and coagulated tissue fragments (i.e., reddish in epithelial and muscularis mucosa, purple in lamina propria and submucosa), easily detectable to identify the photothermally affected area. Brightfield's limited damage analysis of H&E staining was insufficient

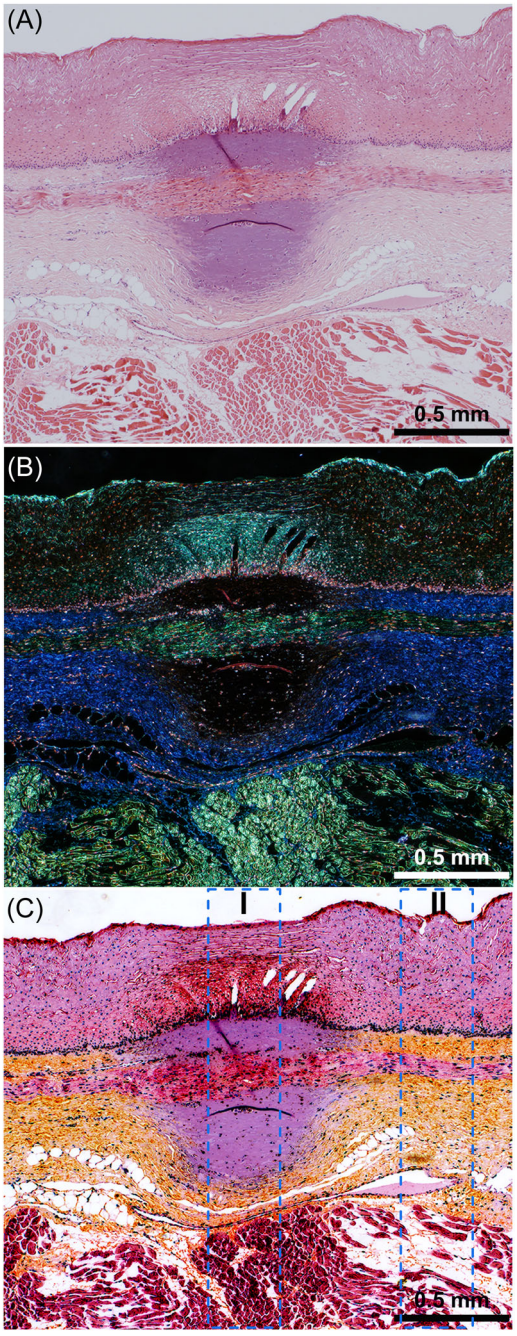


**FIGURE 7** An example of highlighting contrast and morphological information of a thermally damaged area with the color subtraction approach. Samples of the brightfield (A) and darkfield (B) microscopy images of ex vivo sheep esophagus stained with hematoxylin and eosin and the color subtraction result (C) for 284 mW laser power (35.1 W/cm$^2$) at a laser scanning speed of 1 mm/second. Blue dashed rectangles indicate coagulated (I) and uncoagulated control (II) tissue sections further investigated under electron microscopy; ×4 magnification (0.13 NA). Scale bar = 0.5 mm.

to detect accurate margins but the most major thermal injury. Electron microscopy imaging was performed on unstained tissue samples from the consecutive slice to clearly understand and characterize the effect of photothermal coagulation at the cellular level. From the coagulated (Figure 7C,I) and control (i.e., uncoagulated) (Figure 7C,II) regions marked with blue dashed rectangles, a vertical portion of the gold-coated tissue sample was examined from the epithelial layer to the muscle.

Figure 8 shows the block-face scanning electron microscopy (Sigma 500l Zeiss) images acquired at ×1500 magnification from coagulated (I) and control (II) regions. Enlarged views of the circle area from the panels highlight the epithelium, basal lamina, lamina propria, muscularis mucosa, submucosa, and muscle layers and reveal changes compared to control.

After coagulation, the integrity of most of the cells was disrupted, and the cell nucleus or chromatin structure was lost in the epithelial layer. The basal lamina showed similar changes but was milder than the epithelium. Similarly, it was difficult to distinguish cell nuclei or chromatin structures within the basal lamina. Also, the cells were different in that they appeared cubically in uncoagulated tissue, elongated vertically after coagulation. Another profound change manifested in the lamina propria and submucosa, which usually have fibrillar, viscous, and less dense structures, transforming into homogeneous, dense, and opaque structures. Thickening of the muscularis mucosa was observed due to the separation of the muscle fibers forming the internal spaces after coagulation. Tear-like mechanical damage was observed at the intersection of the submucosa and muscle layers caused by high laser energy. The absence of any changes in the muscle layer indicated that the depth of laser-induced damage was limited to the submucosa at 35.1 J/cm$^2$ laser energy density.

## Comparison of the simulation results with ex vivo tissue studies

Finally, we validated the guide map shown in Figure 5 with experimental thermally damaged area results and compared these results directly as a function of energy density (i.e., fluence, J/cm$^2$). Figure 9A shows a reconstructed version of Figure 5 with validation study results for an acceptable irradiance range and surface scanning speeds, given the limited resources for experimental studies. Discrete data sets were interpolated for a seamless display while reconstructing the guide map with simulation and experimental results. The color bar indicates the interpolated laser-induced thermally damaged area.

As a next step, energy density was calculated to compare the simulation results with the experimental results more straightforwardly. Figure 9B demonstrates the logic followed in calculating the fluence to which the tissue is exposed during the laser scan. Energy density was directly proportional to laser power and inversely proportional to beam diameter ($R$) and surface scanning speed ($\vartheta$). This correlation took the scan distance out of the equation with >99% beam overlapping, as in Figure 5.

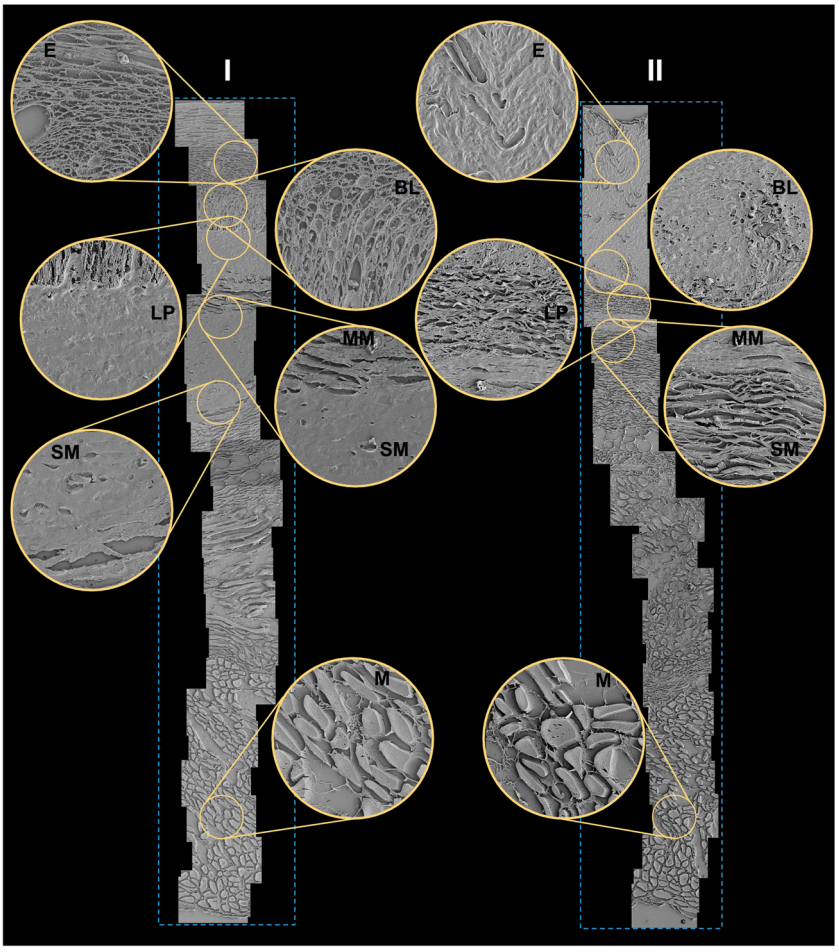


**FIGURE 8** Images of coagulated (I) and uncoagulated control (II) tissue sections were further investigated under the block-face scanning electron microscopy. Enlarged views of the circle area from the panels highlight the epithelium (E), basal lamina (BL), lamina propria (LP), muscularis mucosa (MM), submucosa (SM), and muscle (M) layers and reveal changes compared to control in terms of morphological alterations at the cellular level.

The damaged area plot as a function of energy density in Figure 9C directly compares simulation and experiment results. As before, discrete data sets were interpolated for a seamless plot. The orange line shows the damaged area measured from cross-sectional histology samples obtained during laser scans at different scanning speeds ranging from 0.5 to 2 mm/second, and the orange region represents the standard deviation. The blue dashed line marks the simulation results.

The correlation of simulation and experiment results suggested that thermal damage and laser energy deposited into the tissue are directly related and define laser-induced photothermal coagulation. The results confirmed the onset of acute thermal injury symptoms at 10 J/cm$^2$. Although the fluctuation in the experimental results was obtained within a limited range (25–40 J/cm$^2$), the comparison study showed that the simulation engine generally provided estimates consistent with the ex vivo tissue model. It was determined that the standard deviation of the damaged area measurements increased relatively at an energy density of 60 J/cm$^2$ and above. It was evaluated that the increase in error in area measurements could be due to heat-induced mechanical damage at the intersection of the submucosa and muscle layers at the high laser energy. In Figure 8, for example, heat-induced mechanical damage between the submucosa and muscle layers was observed for laser powers of 284 and 309 mW, which was limiting in defining the area of thermal damage.

## DISCUSSION

Laser-induced photothermal therapy has been used in gastroenterology studies since the late 1970s. In general, several laser types have been used, including argon laser at 514 nm, KTP-YAG laser at 532 nm, and Nd:YAG laser at 1064 nm.[29–31] Studies of the endoscopic laser-induced thermal method were mainly in the case of massive hemorrhage[32] and or the palliation of advanced, inoperable cancers of the upper and lower gastrointestinal tract.[33,34] The method has also played an important role in studies of superficial abnormal tissue treatment,[35,36] such as the management of Barrett's esophagus. Although endoscopic laser therapy has been explored to treat uncomplicated Barrett's mucosa, other thermal ablative methods such as RF ablation and argon plasma coagulation are widely preferred for this purpose. However, the multiple procedures of the contact RF ablation method limit the control of treatment depth. In the noncontact

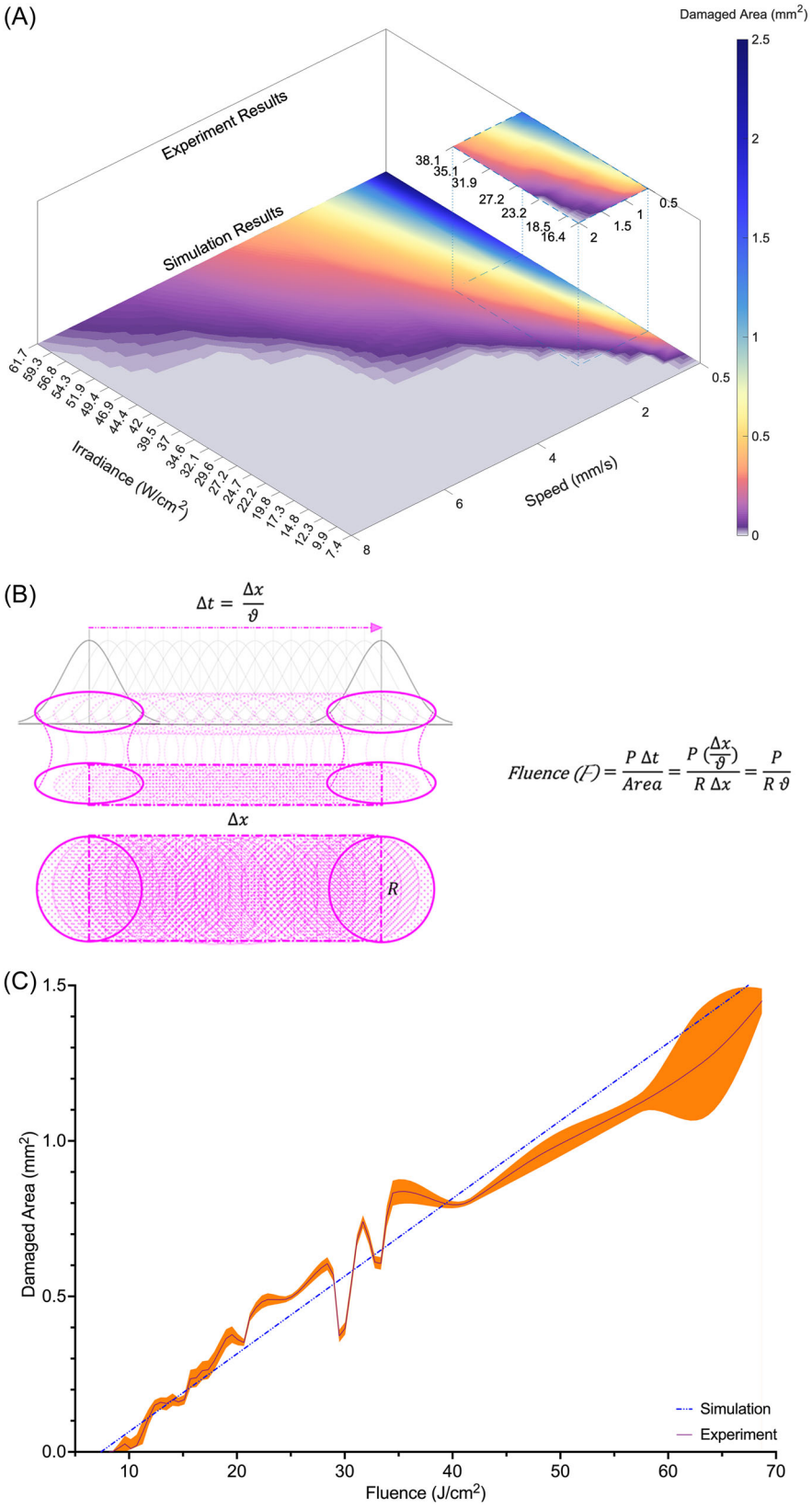


**FIGURE 9** Reconstructed version of the guide map, including validation study results for an acceptable irradiance range and surface scanning speeds given the limited resources for experimental studies (A). Logic calculated the fluence to which the tissue is exposed during the laser scan (B). Energy density is directly proportional to laser power and inversely proportional to beam diameter ($R$) and surface scanning speed ($\vartheta$). This correlation takes the scan distance from the equation with >99% beam overlap. A plot of the damaged area plot as a function of energy density to directly compares simulation (blue dashed line) and experiment results (C). The orange line shows the damaged area measured from cross-sectional histology samples obtained at different scanning speeds ranging from 0.5 to 2 mm/second. The orange region represents the standard deviation. Discrete data sets are interpolated for a seamless plot.

argon plasma coagulation method, the coagulation depth depends on the distance between the probe and the target lesion and the application time. For these reasons, the experience and technique of the operator are very important for successful treatment in both methods. Besides, an unconfined depth of thermal effect produced can intrinsically lead to the risk of muscle scarring or even perforation, resulting in treatment failure.

Endoscopic management of superficial abnormal tissue remains a valid challenge. Even though laser therapy (i.e., laser-induced photothermal coagulation) has been gradually abandoned to treat superficial abnormal tissues,[37] it still has the potential for high safety and efficacy with minimal side effects. In addition, developments in optical imaging, fiber optical components, and diode laser technologies, which enable new probe designs, will bring laser therapy to the agenda more strongly again. The problem is that parameters such as laser irradiance and energy density are chosen quite empirically without adequate comparison with theory. In this context, it may be of interest to develop a numerical model simulating laser-induced photothermal mucosa coagulation.

This article presents a computer simulation engine that predicts laser-induced thermal damage by calculating the energy deposition of absorbed photons in the mucosa tissue layer. The developed computational model was able to map the area of irreversible thermal damage with accurate depth. The guide map simplified a matrix of treatment parameters (such as laser irradiance, beam diameter, and surface scanning speed) for successful photothermal mucosal therapy. In addition, the guide map created for a CW laser operated at 1505 nm in the ex vivo sheep model was verified. It has been noted that the theoretical and experimental data compared in terms of energy density are highly overlapping.

The various assumptions and limitations of the study should be discussed. First, the absorption and scattering coefficients and thermal properties of the tissue model were assumed to be constant over time during simulation studies. This assumption may be a reasonable and practical approximation for tissue-laser interaction that does not cause a considerable temperature variation. However, this can limit the simulation run, especially in the case of large thermal gradients where the tissue undergoes a phase change.

Second, soft tissue contains 70% water, and water can be the primary chromophore for soft tissues in the near-IR spectrum. Therefore, we hypothesized that the optical properties might not differ much between the layers of the esophagus. Nevertheless, these data may be needed to fine-tune the simulation model. However, the literature lacks optical and thermal properties for all layers of the esophagus.

Third, compared to pulsed lasers, the diode laser operating in CW mode over a telecommunications wavelength range stood out for its relative cost-effectiveness and potential damage reduction in optical fiber evaluations. However, completing the validation work with a CW laser can be limiting. Thus, the work can be expanded by considering the pulsed laser case.

Fourth, the effect of surrounding uncoagulated tissue responses on healing was not considered in the model at this stage. Similarly, autolytic processes (i.e., postmortem degeneration and necrosis) in the ex vivo tissue were ignored in the study. Although the ex vivo tissue model provides relatively sufficient thermal response data, the notable importance of the in vivo animal model, which is beyond the scope of this study, is noted for future studies, including the analysis of acute and chronic thermal injury. Additionally, the effect of convective blood flows on mucosal coagulation can be analyzed by adding forced convection as a layer to the tissue model in simulation.

Finally, a more rigorous histological analysis of thermal damage to the esophagus is required for the in vivo animal model and a long-term study to determine the extent of progressive chronic damage. For histological analysis, nitroblue tetrazolium chloride staining, active for the cytoplasmic marker enzyme lactate dehydrogenase, can be used to provide high contrast between healthy tissue and laser-induced thermally damaged tissue.

## CONCLUSION

The photothermal coagulation technique, which is included in the endoscopic thermal therapy method, can adequately respond to the needs of superficial treatments in the gastrointestinal tract. The potential of the photothermal coagulation technique can be reassessed with advances in optical imaging, fiber optic components, and diode laser technology at the telecommunication wavelength range. The presented results have demonstrated that the simulation engine can be a valuable tool to optimize coagulation variables to eradicate superficial abnormal tissue structures. Validation studies performed for a laser wavelength 1505 nm in ex vivo sheep esophagus support this assumption. The developed simulation engine can be enriched for different laser wavelengths combined with a suitable in vivo model for further studies.

## ACKNOWLEDGMENTS

The authors thank Defne Ozturk (electron microscopy) and Ece Uzun (histology) from the IBG core facilities.

## CONFLICT OF INTEREST

The authors declare no conflict of interest.

## ORCID

*Merve Turker-Burhan* https://orcid.org/0000-0001-7101-3835
*Nevin Ersoy* http://orcid.org/0000-0002-6992-8451
*Husnu A. Bagriyanik* http://orcid.org/0000-0003-4064-7637
*Serhat Tozburun* http://orcid.org/0000-0002-4397-4011

## REFERENCES

1. Liao D-H, Zhao J-B, Gregersen H. Gastrointestinal tract modelling in health and disease. World J Gastroenterol. 2009;15(2):169–76.

2. Chung C-S, Wang H-P. Screening for precancerous lesions of upper gastrointestinal tract: from the endoscopists' viewpoint. Gastroenterol Res Pract. 2013;2013:1–18.
3. Martinucci I, de Bortoli N, Russo S, Bertani L, Furnari M, Mokrowiecka A, et al. Barrett's esophagus in 2016: from pathophysiology to treatment. World J Gastrointest Pharmacol Ther. 2016;7(2):190–206.
4. Garud SS, Willingham FF, Cai Q. Diagnosis and management of Barrett's esophagus for the endoscopist. Therap Adv Gastroenterol. 2010;3(4):227–38.
5. Watson TJ. Endoscopic therapies for Barrett's neoplasia. J Thorac Dis. 2014;6(Suppl 3):298–308.
6. Shaheen NJ, Sharma P, Overholt BF, Wolfsen HC, Sampliner RE, Wang KK, et al. Radiofrequency ablation in Barrett's esophagus with dysplasia. N Engl J Med. 2009;360(22):2277–88.
7. Johanns W, Luis W, Janssen J, Kahl S, Greiner L. Argon plasma coagulation (APC) in gastroenterology: experimental and clinical experiences. Eur J Gastroenterol Hepatol. 1997;9(6):581–7.
8. Kallam A, Alsop BR, Sharma P. Limitations of endoscopic ablation in Barrett's esophagus. Expert Rev Gastroenterol Hepatol. 2015;9(4):487–96.
9. Hohmannohmann M, Lengenfelder B, Kanawade R, Klämpfl F, Douplik A, Albrecht H. Measurement of optical properties of pig esophagus by using a modified spectrometer set-up. J Biophotonics. 2018;11(1):e201600187.
10. Ribeiro SR, Pinto Júnior PE Jr, Miranda AC, Bromberg SH, Lopasso FP, Irya KSH. Weight loss and morphometric study of intestinal mucosa in rats after massive intestinal resection: influence of a glutamine-enriched diet. Rev Hosp Clin Fac Med Sao Paulo. 2004;59(6):349–56.
11. Schena E, Saccomandi P, Fong Y. Review laser ablation for cancer: past, present and future. J Funct Biomater. 2017;8(2):1–15.
12. Marmur ES, Schmults CD, Goldberg DJ. A review of laser and photodynamic therapy for the treatment of nonmelanoma skin cancer. Dermatol Surg. 2004;30:264–71.
13. Lee H, Lee Y, Song C, Cho HR, Ghaffari R, Choi TK, et al. An endoscope with integrated transparent bioelectronics and theranostic nanoparticles for colon cancer treatment. Nat Commun. 2015;6:1–10.
14. Dix T, Barr H. Photothermal ablation of metaplastic columnar-lined (Barrett's) esophagus, experimental studies for safe endoscopic laser therapy. Proc SPIE. 1996;2922:2750280.
15. Salo JA, Salminen JT, Kiviluoto TA, Nemlander AT, Rämö OJ, Färkkilä MA, et al. Treatment of Barrett's esophagus by endoscopic laser ablation and antireflux surgery. Ann Surg. 1998;227(1):40–4.
16. Bowers SP, Mattar SG, Waring PJ, Galloway K, Nasir A, Pascal R, et al. KTP laser ablation of Barrett's esophagus after anti-reflux surgery results in long-term loss of intestinal metaplasia. potassium-titanyl-phosphate. Surg Endosc. 2003;17(1):49–54.
17. Wilson BC, Adam G. A Monte Carlo model for the absorption and flux distributions of light in tissue. Med Phys. 1983;10(6):824–30.
18. Wang LH, Jacques SL, Zheng Z. MCML—Monte Carlo modeling of light transport in multi-layered tissues. Comput Methods Programs Biomed. 1995;47(2):131–46.
19. Pennes HH. Analysis of tissue and arterial blood temperature in the resting human forearm. J Appl Phys. 1948;1:93–102.
20. Henriques FC, Moritz AR. Studies of thermal injury: I. The conduction of heat to and through skin and the temperatures attained therein. A theoretical and an experimental investigation. Am J Pathol. 1947;23(4):531–49.
21. Bashkatov AN, Genina EA, Kochubey VI, Gavrilova AA, Kapralov SV, Grishaev VA, et al. Optical properties of human stomach mucosa in the spectral range from 400 to 2000 nm: prognosis for gastroenterology. Med Laser Appl. 2007;22(2):95–104.
22. Collins CM, Smith MB, Turner R. Model of local temperature changes in brain upon functional activation. J Appl Physiol. 2004;97:2051–55.
23. Pearce JA. Relationship between Arrhenius models of thermal damage and the CEM 43 thermal dose. Proc. SPIE 7181, Energy-based Treatment of Tissue and Assessment V (Ed: Ryan TP), 2009.
24. Liu JB, Miller LS, Goldberg BB, Feld RI, Alexander AA, Needleman L, et al. Transnasal US of the esophagus: preliminary morphologic and function studies. Radiology. 1992;184(3):721–27.
25. Taniguchi DK, Martin RW, Trowers EA, Silverstein FE. Simultaneous M-mode echoesophagram and manometry in the sheep esophagus. Gastrointest Endosc. 1995;41(6):582–6.
26. Glanzmann TM, Zellweger MP, Borle F, Conde R, Radu A, Ballini JP, et al. Assessment of a sheep animal model to optimise photodynamic therapy in the oesophagus. Lasers Surg Med. 2009;41(9):643–52.
27. Radu A, Conde R, Fontolliet C, Wagnieres G, Van den Bergh H, Monnier P. Mucosal ablation with photodynamic therapy in the esophagus: optimization of light dosimetry in the sheep model. Gastrointest Endosc. 2003;57(7):897–905.
28. Hale GM, Querry MR. Optical constants of water in the 200 nm to 200 μm wavelength region. Appl Opt. 1973;12(3):555–63.
29. Fleischer D. Endoscopic laser therapy for gastrointestinal disease. Arch Intern Med. 1984;144(6):1225–30.
30. Hunter JG. Endoscopic laser applications in the gastrointestinal tract. Surg Clin North Am. 1989;69(6):1147–66.
31. Schwesinger WH. Laser treatment of esophageal and gastric lesions. Surg Clin North Am. 1992;72(3):581–95.
32. Swain CP. Laser therapy for gastrointestinal bleeding. Gastrointest Endosc Clin N Am. 1997;7(4):611–39.
33. Brunetaud JM, Maunoury V, Cochelard D. Lasers in digestive endoscopy. J Biomed Opt. 1997;2(1):42–52.
34. Courtney ED, Raja A, Leicester RJ. Eight years experience of high-powered endoscopic diode laser therapy for palliation of colorectal carcinoma. Dis Colon Rectum. 2005;48(4):845–50.
35. Weston AP. Use of lasers in Barrett's esophagus. Gastrointest Endosc Clin N Am. 2003;13(3):467–81.
36. Polese L, Angriman I, Scarpa M, Pagano D, Parente P, Erroi F, et al. Diode laser treatment of Barrett's esophagus: long-term results. Lasers Med Sci. 2011;26(2):223–8.
37. Rouphael C, Anil Kumar M, Sanaka MR, Thota PN. Indications, contraindications and limitations of endoscopic therapy for Barrett's esophagus and early esophageal adenocarcinoma. Therap Adv Gastroenterol. 2020;13:1756284820924209.


**How to cite this article:** Turker-Burhan M, Ersoy N, Bagriyanik HA, Tozburun S. Guide mapping for effective superficial photothermal coagulation of the esophagus using computer simulations with ex vivo sheep model validation study. Lasers Surg Med. 2022;54:1116–1129.
https://doi.org/10.1002/lsm.23595